



# Effect of Initial Microstructure on the Hot Deformation Behavior and Microstructure Evolution of Aluminum Alloy AA2060

Chaoyang Li<sup>1,2</sup> · Guangjie Huang<sup>1</sup> · Lingfei Cao<sup>1,3</sup> · Ruoxi Zhang<sup>2</sup> · Yu Cao<sup>1</sup> · Bin Liao<sup>4</sup> · Lin Lin<sup>2</sup>

Received: 12 February 2021 / Accepted: 1 April 2021 / Published online: 3 September 2021  
© The Korean Institute of Metals and Materials 2021

## Abstract

The microstructure evolution and hot deformation behavior of a Li-containing aluminum alloy AA2060 with different initial microstructure (homogenized vs. pre-rolled) were studied by isothermal hot deformation. The tests were performed within a wide range of deformation temperatures of 370–490 °C and strain rates of 0.01–10 s<sup>-1</sup>. Results show that the stress drop ratio of the pre-rolled specimen is higher than that of the homogenized one under the same deformation condition. Microstructure were analyzed on the thermal processing maps in unstable and optimum processing domain, and a higher dynamic recrystallization fraction can be observed in the pre-rolled specimen that has more substructures and smaller grains. Four types of the dynamic recrystallization were observed and the mechanism for deformation softening was discussed in this work.

**Keywords** Aluminum alloy AA2060 · Flow behavior · Processing map · Dynamic recrystallization

## 1 Introduction

In modern industrial production, the structural materials for aviation industry should have outstanding combinations of engineering properties and also enable lightweight and durable structure to be manufactured, which leads to the rapid development of aluminum alloys containing Li. Compared with the conventional ones, the newly developed aluminum alloys containing Li are basically featured by the low density, high specific strength, low fatigue crack growth, high corrosion resistance and good performance at low temperature [1]. It is widely accepted that the AA2060 alloy, which has a higher Cu/Li ratio but lower contents of elements such

as Li, Fe, Ag, and Si, was a typical third-generation Al–Li alloy for producing wings and fuselage skins in aircraft [2].

Generally, hot rolling is crucial for the manufacturing of AA2060 alloy sheet. During this hot processing, the dynamic recrystallization (DRX) and dynamic recovery (DRV) are prone to take effect as a significant restoration process, and able to tailor the deformation microstructure to improve mechanical properties of the final products. Therefore, to understand the hot deformation behaviors and evolution of microstructure of AA2060 alloy under different loading conditions and service environment are of great interest for both industrial practice and academic research. Ou et al. [7] studied the homogenized and air-cooled AA2060 alloy, and hot compressed it at 300–500 °C with strain rates at 0.01–10 s<sup>-1</sup>. The results showed that DRV was the main dynamic softening mechanism associated with the activation energy of 205 kJ/mol. Zhu et al. [8] carried out the hot compression from 340 °C to 500 °C with a temperature interval of 40 °C and strain rates of 0.001–10 s<sup>-1</sup>. Experimental results show that both DRV and DRX occurred during the hot deformation of AA2050 alloy, where DRX played a great role when it was deformed at a higher temperature and low strain rate, and dynamic precipitation (DPN) enhanced the tendency to DRX. The activation energy for hot working was calculated as 294.117 kJ/mol. Effects of deformation parameters such as heating rate, flow stress, strain rate, strain, temperature on microstructure, e.g. second phase particles, were

✉ Guangjie Huang  
gjhuang@cqu.edu.cn

✉ Lingfei Cao  
caolingfei@cqu.edu.cn

<sup>1</sup> International Joint Laboratory for Light Alloys (Ministry of Education), College of Materials Science and Engineering, Chongqing University, Chongqing 400044, China

<sup>2</sup> Southwest Aluminum (Group) Co., Ltd, Chongqing 401326, China

<sup>3</sup> Shenyang National Laboratory for Materials Science, Chongqing University, Chongqing 400044, China

<sup>4</sup> Nannan Aluminum Co., Ltd, Nanning 530031, China

adjusted by the design of deformation passes [9]. The studies [10] on the alloy Al–Cu–Li–Mg–Ag presented that DRV was the main mechanism for deformation softening, and the optimum deformation condition for this materials was at a temperature range of 440–470 °C and strain rates range of 0.01–0.03 s<sup>-1</sup>, in which continuous dynamic recrystallization (CDRX) and discontinuous dynamic recrystallization (DDRX) were confirmed as the main recrystallization mechanism at higher lnZ and lower lnZ values, respectively. These results have revealed that the increasing number of sub-grain and the frequency of recrystallization ratio may increase with (a) particles stimulate nucleation (PSN), (b) increasing deformation temperature, (c) increasing dislocation density, (d) decreasing strain rate, (e) increasing the amount of deformation [7–12].

At present, in most cases the thermal–mechanical simulation work has been executed on samples homogenized after casting, which is called as conventional thermo-mechanical process (CTMP process, as shown in Fig. 1 a). In industrial practice, the cast ingot may also be pre-rolled to reduce the thickness, then transported or stored in the naturally aged condition before further rolling. This process is called the intermediate thermo-mechanical process (ITMP process, Fig. 1 b), and Ye et al. [13] applied this technique to obtain fine grains about 10 μm in size. The variety of thermo-mechanical processes make it difficult to figure out the full frame of the hot deformation behavior and microstructure changes involved. For these alloys whether they were homogenized or pre-rolled and naturally aged (T1), different flow stress behavior and recrystallization mechanisms may exist. Therefore, it is important to understand the hot workability of the alloy materials under different deformation conditions to provide possibilities for production design.

In this work, the AA2060 alloy containing Li was processed under two different conditions (i.e., homogenized and pre-rolled (T1)), and then its hot deformation behavior was investigated by using isothermal compression tests at elevated temperatures. Besides, the hot workability of AA2060 alloy has been evaluated to optimize the deformation parameters by using processing maps. Finally, the corresponding microstructure evolution has been discussed to reveal the recrystallization mechanism in this alloy.

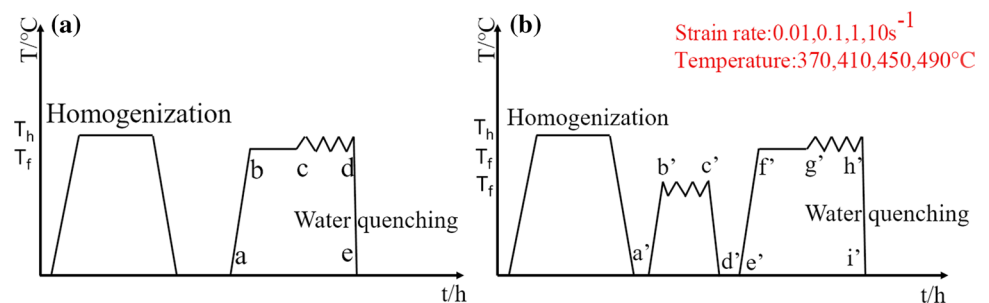
## 2 Experiments and Materials

The nominal composition of AA2060 alloy referred in this work is: Al-3.8Cu-0.3Mn-0.8 Mg-0.4Zn-0.13Zr-0.7Li-0.4Ag, and the remaining elements of Fe, Si, Ti are less than 0.1 wt%. The alloy was semi-continuously cast into ingots which were approximately 300 mm × 1200 mm × 4000 mm in dimension. The ingots were processed through the two-stage homogenization treatment at 460 °C for 4 h followed by 495 °C for 24 h, and then furnace cooled. Afterward, part of them were pre-deformed by 50% at a deformation temperature of 400 °C, and then naturally aged for exceed 3 months at room temperature.

Cylindrical specimens (10 mm in diameter and 15 mm in height) were machined from the homogenized ingot and pre-deformed material through the thickness direction. The compression tests were executed by using a thermal mechanical simulator (Gleeble-3800, DSI, USA) within a wide range (370–490 °C with an interval of 40 °C at strain rates of 0.01–10 s<sup>-1</sup>). All samples were heated at a rate of 5 °C/s to the deformation temperature and held for 180 s. The samples were deformed on the height direction by 60%, and then quenched by water at room temperature to retain their microstructure in the hot deformed state.

The deformed samples were then halved along the compression center axis. Scanning electron microscopy (SEM, TESCAN Vega 3, Czech Republic) equipped with an electron backscatter diffraction (EBSD, Oxford Instruments, UK) detector was utilized for microstructure characterization, operated at 20 kV. The observed surface was ground mechanically (emery paper, 280# to 3000#) and then electro-polished by using a 10% perchloric acid and 90% alcohol at 20 V for 15 s. The data of EBSD were analyzed by using the commercial software HKL Channel 5.

**Fig. 1** The thermo-mechanical treatment diagrams of two processes: **a** CTMP; **b** ITMP



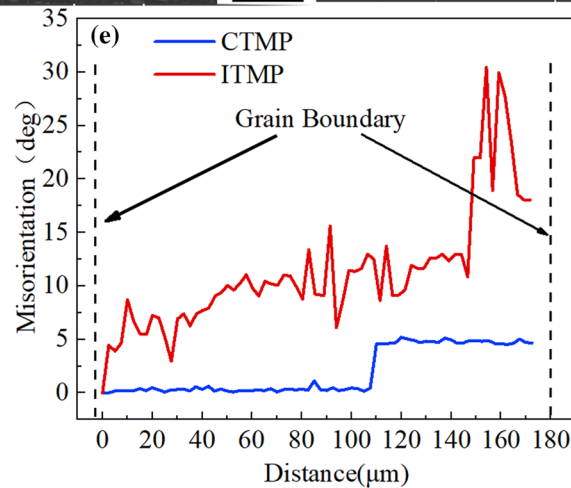
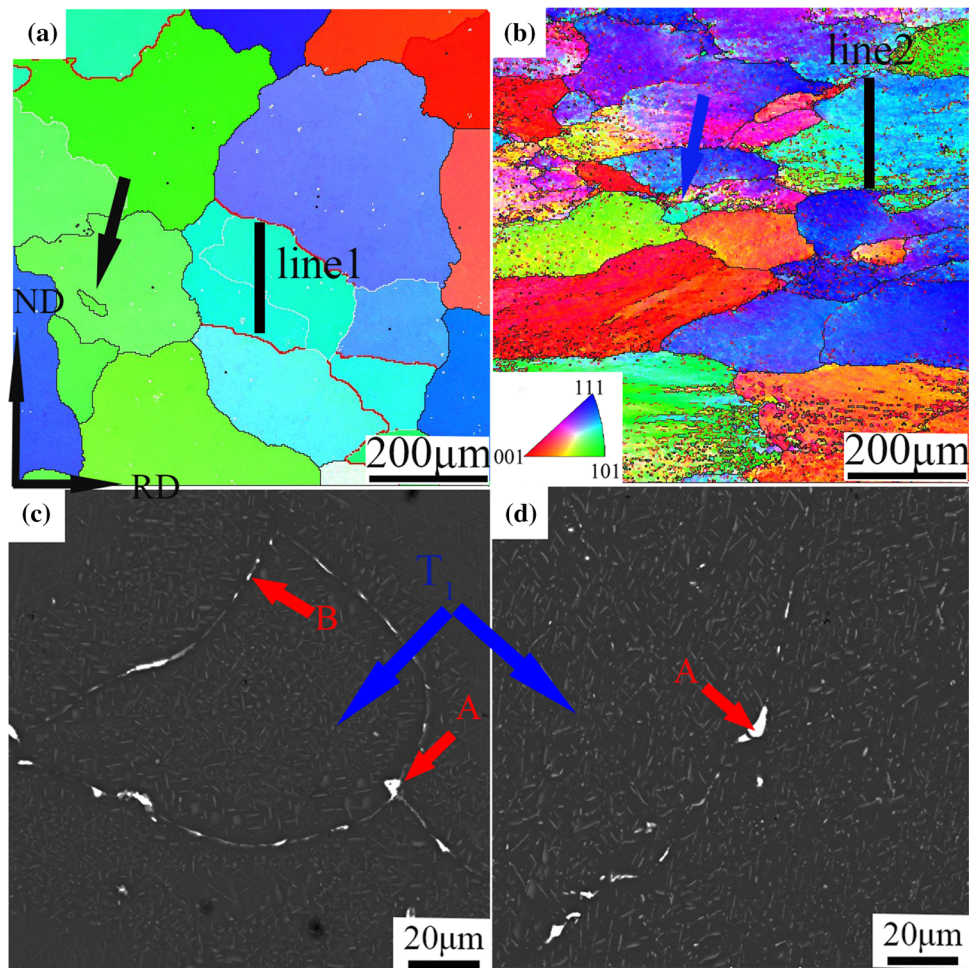
### 3 Results and Discussion

#### 3.1 Initial Microstructure of Two Processes

The initial microstructure of samples before deformation in CTMP and ITMP processes are depicted in Fig. 2. It can

be seen that in the homogenization condition, the grains are equiaxed with an average grain size of 122  $\mu\text{m}$ . A few new grains appear at the grain interior and the corners of the triple junction of grain boundaries, as marked in the EBSD IPF figure by the black arrow in Fig. 2 a. The pre-rolled (T1) specimen was taken from the point d' in Fig. 1 b. It is clear that the pre-rolled grains become flat

**Fig. 2** The microstructure before deformation CTMP **a, c** and ITMP **b, d, e** point-to-origin misorientation profile across deformed grains (thick black lines shown in **a** and **b**)



and elongated and the average grain size is about 78  $\mu\text{m}$ . Among grains, some recrystallized grains (pointed by blue arrows) are observed in Fig. 2 b. The local misorientation of CTMP and ITMP samples deformed were examined and shown in Fig. 2 e, which represents the cumulative misorientation along the grain boundary (thick black lines in Fig. 2 a and b). ITMP samples have grain misorientation exceeding  $15^\circ$ , which indicates that the effects of dislocation multiplication is obvious with the increase of deformation. Comparably, the grain misorientation of CTMP sample is not higher than  $5^\circ$ . This corresponds to the dislocation-free grains, which are consistent with the results of T.J. Ruggles et al. [14]. In addition, the initial microstructure shows random orientations in both homogenized and pre-rolled samples, and no obvious texture is observed.

The SEM backscattered image of the as-homogenized and pre-deformed samples show a large number of coarse particles  $T_1$  ( $\text{Al}_2\text{CuLi}$ ) (pointed by blue arrows in Fig. 2 c, d), which are consistent with the results of Wang et al. [15]. The average size of the coarsest  $T_1$  particles in this work is calculated as 0.8  $\mu\text{m}$ , which is less than the critical size (1  $\mu\text{m}$ ) for the occurrence of particle stimulated nucleation (PSN) [16]. Therefore, the coarse  $T_1$  phases are less effective to trigger PSN. In the as-homogenized samples, the residual  $\text{Al}_2\text{Cu}$  (Mg) phases are continuously distributed along the grain boundaries (A and B in Table 1), while a large number of  $T_1$  coarse particles are inside the grains. In the pre-deformed samples, the interdendritic second phases become discontinuous, and a few residual  $\text{Al}_2\text{Cu}$  phases remain in the grain boundaries. Therefore, the main difference in the initial microstructure of as-homogenized and pre-deformed samples is the type of residual phases and the grain size.

### 3.2 Typical true stress-true strain response

Figure 3 illustrates the typical flow stress curves of AA2060 alloy in different deformation conditions i.e., the deformation strain rate 0.01–10  $\text{s}^{-1}$  at temperatures between 370  $^\circ\text{C}$  and 490  $^\circ\text{C}$  in the CTMP and ITMP process, respectively. Their initial microstructure is different, but both specimens show that the flow stress is higher when the deformation temperature is relatively lower and strain rate is constant. At the beginning stage of compression, for all samples the flow stress curves are leveled off after they initially increase

sharply to attaining the peak value. This is caused by balance resulting from work hardening and softening. Afterwards, when the deformation temperature increases from 370  $^\circ\text{C}$  to 490  $^\circ\text{C}$ , the stress level decreases gradually to a steady state with a less visible stress fluctuation, indicating that dynamic softening and work hardening have reached a dynamic balance. The average difference of stress level is about 10 MPa at the deformation strain rate 0.01  $\text{s}^{-1}$  and 370  $^\circ\text{C}$  (Fig. 3 a,b). Moreover, the average stress level is roughly 2–3 MPa difference at a higher deformation temperature of 490  $^\circ\text{C}$  and the same strain rates 0.01  $\text{s}^{-1}$  (Fig. 3 a,b). Meanwhile, it can be found that leading to a significantly increase of flow stress with the increase of strain rate. The flow stress level is about 60–90 MPa difference at deformation temperature from 370  $^\circ\text{C}$  to 490  $^\circ\text{C}$ , which the strain rates 0.01  $\text{s}^{-1}$  and 10  $\text{s}^{-1}$ , respectively. This is mainly because high strain rate for accelerates the working hardening effect in the deformation process (Fig. 3 a, g; b, h). Such a difference is due to a continuous dynamic softening behavior, comparatively, there are high dislocation density in ITMP process. It is indicated that the flow stress softening behavior are influenced by to the DRV and DRX in the hot deformation, where DRV may occur at a lower deformation temperature, and DRX may be the dominant softening mechanism at a high deformation temperature and low strain rate (Fig. 3. a and b). In this case more recrystallization is possible [17]. There are more substructure grain in the pre-rolled ( $T_1$ ) sample for the ITMP process than the homogenized one for the CTMP process, so the former has higher dislocation accumulation and stored energy, as well as more sub-grains, which impacts the softening mechanism.

It is clearly indicated that the material has different softening characteristics in different deformation conditions. In order to show the above difference, the flow stress decline ratio map is depicted in Fig. 4. The relative softening rate  $M_s$  can be used to characterize the softening level of the material [18].

$$M_s = 100\% \times \frac{N_i - N_f}{N_f} \quad (1)$$

Here a true strain condition of 0.9 is chosen for discuss,  $N_i$  is the value of flow stress at the end of deformation, and  $N_f$  is the peak value on the flow stress curves.

As shown in Fig. 4 a and b, it can be seen clearly that the most significant decrease of flow stress occurs at low strain rates from 0.01  $\text{s}^{-1}$  to 0.1  $\text{s}^{-1}$  ( $\log \dot{\epsilon} = -2$  to  $-1$ ) (the blue region) and high strain rate of 1–10  $\text{s}^{-1}$  ( $\log \dot{\epsilon} = -0.5$  to 1) (the red region). The flow stress drops more in the homogenized (CTMP) than the pre-rolled ( $T_1$ ) (ITMP) condition when the deforming temperature is within the range of 410–450  $^\circ\text{C}$ , while the flow stress with the deformation temperature between 370  $^\circ\text{C}$  and 410  $^\circ\text{C}$  shows opposite

**Table 1** Composition of the second phase in the initial microstructure of CTMP and ITMP samples by EDS analysis (at%)

Point	Al	Cu	Mg	possible phases
A	69.5	30.5		$\text{Al}_2\text{Cu}$
B	50.4	38.0	12	$\text{Al}_2\text{Cu}(\text{Mg})$

tendency. The highest value of relative softening rate  $M_s$  occurs in the temperature between 380 °C to 450 °C at strain rates range of 0.01 s<sup>-1</sup>–0.0316 s<sup>-1</sup> (log  $\dot{\epsilon}$  = -2 to -1.5) in the homogenized condition. However for the sample and pre-rolled, the highest values appear at temperatures between 370 °C and 390 °C for strain rates between 0.01 s<sup>-1</sup> to 0.1 s<sup>-1</sup> (log  $\dot{\epsilon}$  = -2 to -1) and from 370 °C to 420 °C for strain rates between 3.16 s<sup>-1</sup> and 10 s<sup>-1</sup> (log  $\dot{\epsilon}$  = 0.5 to 1).

From the data analysis above, the pre-rolled sample during hot deformation has relatively higher  $M_s$  values than the homogenized one, which indicates that a large number of sub-grains leads to softening at a low strain rate or high temperature. The pre-rolled materials have massive dislocation congestion, and it can transform more recrystallization grains at low strain rate and high temperature. However, when the alloy is deformed condition at a lower temperature or higher strain rate, it can infer the nucleating energy of sub-grains to transform into equiaxed grains [19]. Therefore, the values of  $M_s$  are corresponding to multifarious deformation condition softening mechanism, which will be discussed in the chapters below.

### 3.3 Constitutive Equation and Thermal Processing Map

During hot working at high temperature, the relationship among strain rate, flow stress and temperature can be expressed by using the exponential function, power function and hyperbolic sine, involving activation energy in the conditions of low stress, high stress and all stresses as follows [17, 20]:

$$\dot{\epsilon} = A_1 \sigma^{n_1} \exp\left[\frac{-Q}{RT}\right] \quad (\alpha\sigma < 0.8) \quad (2)$$

$$\dot{\epsilon} = A_2 \exp(\beta\sigma) \exp\left[\frac{-Q}{RT}\right] \quad (\alpha\sigma < 1.2) \quad (3)$$

$$\dot{\epsilon} = A[\sinh(\alpha\sigma)]^n \exp\left[\frac{-Q}{RT}\right] \quad (\text{for all}) \quad (4)$$

where  $n_1$ ,  $n$ ,  $\alpha$ ,  $\beta$ ,  $A_1$  and  $A_2$  are the material constants.

The ratio can be determined by the expression of  $\alpha = \beta/n_1$ ,  $R$  is the gas constant,  $T$  is the absolute temperature (K),  $Q$  is the activation energy (kJ·mol<sup>-1</sup>) and  $\dot{\epsilon}$  is the strain. Zener and Holomon proposed using the  $Z$  parameter to describe the influence of strain rate and deforming temperature on flow stress. The expression is as follows [7, 9, 21]:

$$Z = \dot{\epsilon} \exp\left[\frac{Q}{RT}\right] \quad (5)$$

Getting the logarithm of both sides of Eqs. (2) and (3), the relationships of  $\ln \dot{\epsilon} - \ln \sigma$ ,  $\ln \dot{\epsilon} - \sigma$  can be plotted. Therefore, the material constants of  $\alpha$ ,  $\beta$ ,  $n_1$  can be determined respectively by calculating the average slopes in the plots.

Then, for the given strain rate, the calculated value of  $Q$  can be received from the true stress – true strain curves by using the representation [22]:

$$Q = R \left\{ \frac{\partial \ln \dot{\epsilon}}{\partial \ln[\sinh(\alpha\sigma)]} \right\}_T \left\{ \frac{\partial \ln[\sinh(\alpha\sigma)]}{\partial (1/T)} \right\}_\dot{\epsilon} = RnS \quad (6)$$

where  $n$  and  $S$  are material constants,  $\sigma$  is the true stress.

According to Eq. (4), the value of  $n$  and  $S$  can be obtained from the slope of every single line in  $\ln \sinh(\alpha\sigma^{-1}/T$  and  $\ln \dot{\epsilon} - \ln \sinh(\alpha\sigma)$  plots by using linear fitting method, then substituting the average value of  $n$  and  $S$  into Eq. (6). The average of activation energy for the CTMP and ITMP specimens are 135.2KJ/mol and 123.1KJ/mol respectively. The cause of the lower value of  $Q$  for the ITMP condition is that the initial banded grains are almost completed replaced by fine recrystallized grains during the deformation, due to dynamic softening [23, 24].

As shown in Fig. 5,  $Z$  is defined as the temperature compensated strain rate for both homogenized and pre-rolled materials. It can be demonstrated that with the changing of  $\ln Z$ , the microstructure and flow stress exhibit different characteristics. At a high  $\ln Z$  value, the DRV is expansive for dislocations to climb more and increase little by little the misorientation of low-angle boundaries [11]. However, at a low  $\ln Z$  value, the formation of new grains is influenced by CDRX [25]. In addition, the value of  $\ln Z$  can be inferred from characteristics on the true strain- true stress curves as presented in Fig. 3. From the true stress and true strain changes at 370 °C and 490 °C with a strain rate of 0.01 s<sup>-1</sup>, it shows that at the same temperature and strain rate, the value of  $\ln Z$  for the homogenized sample is higher than pre-rolled one. Meanwhile the stress is also higher. It is reasonable to deduce that the pre-rolled material forms a large amount of substructure, and the softening mechanism is mainly DRX. In this case sub-grains can be likely shifted into high angle grain boundaries, so the ITMP sample have more sub-grains growing into recrystallized grains, which is higher than CTMP sample during deformation. Such result can also interprets why the value of  $\ln Z$  of the pre-rolled material can be lower.

The processing maps can be established by using dynamic materials model (DMM) [26], which is commonly used in various metallic materials [22, 27]. The processing maps are the superimposition of power dissipation efficiency map and instability map, which can help to confirm the optimal domains for the hot deformation of the material, thus to acquire its workability. Figure 6 represents the processing maps at temperatures between 370 °C

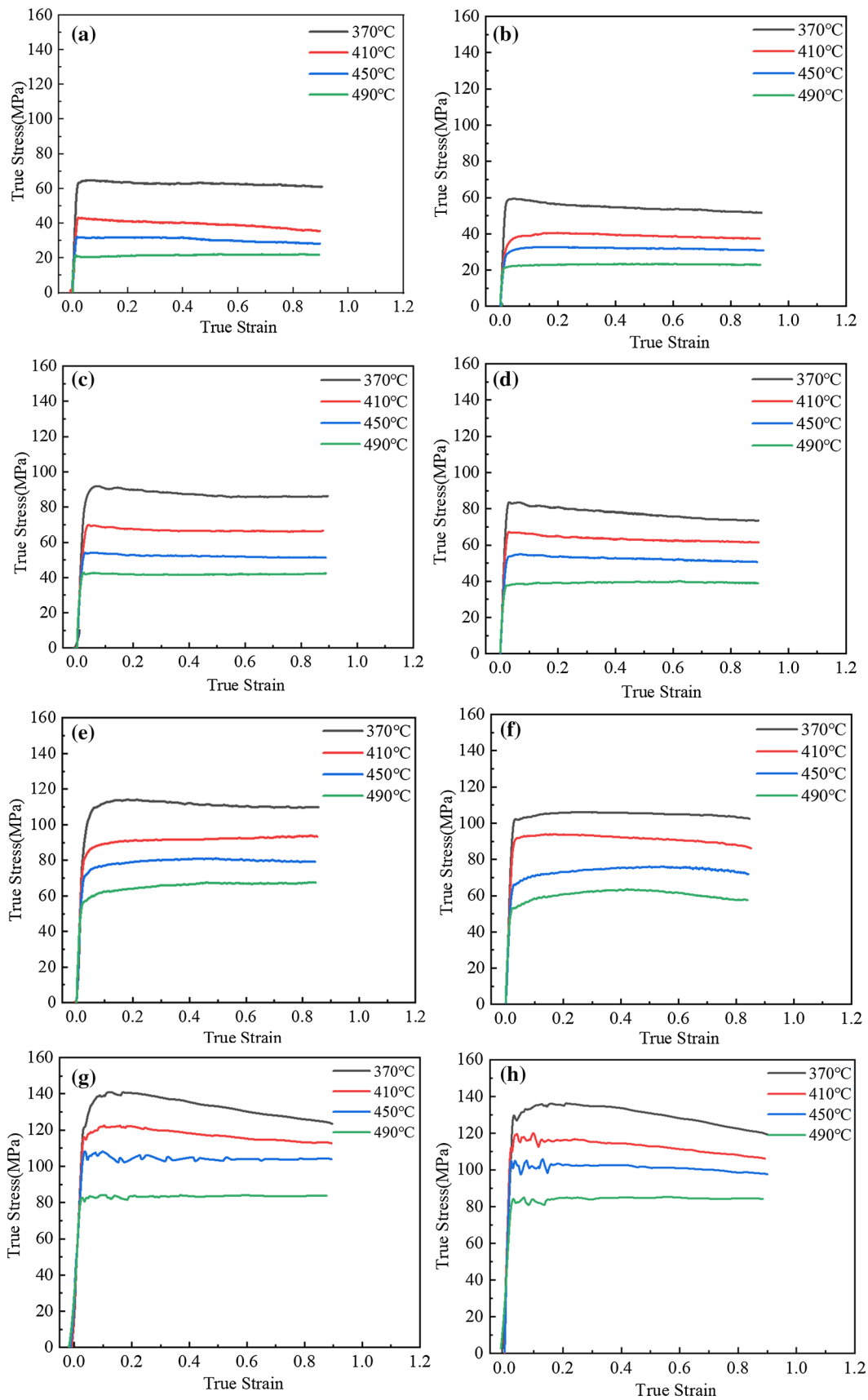


**Fig. 3** Typical true stress-true strain curves of CTMP and ITMP sample at condition a strain rate, **b**  $\dot{\epsilon}=0.01 \text{ s}^{-1}$ , **c**, **d**  $\dot{\epsilon}=0.1 \text{ s}^{-1}$ , **e**, **f**  $\dot{\epsilon}=1 \text{ s}^{-1}$ , **g**, **h**  $\dot{\epsilon}=10 \text{ s}^{-1}$ ; **a**, **c**, **e**, **g** CTMP, **b**, **d**, **f**, **h** ITMP

and 490 °C and strain rates from 0.01 s<sup>-1</sup> to 10 s<sup>-1</sup> (log  $\dot{\epsilon} = -2$  to 1) at condition a true strain of 0.9. The proportion of power dissipation by the microstructure change during the deformation process can be obtained. The power dissipation efficiency  $\eta$  is expressed as [28]

$$\eta = \frac{J}{J_{\max}} = \frac{2m}{1+m} \quad (7)$$

where  $m$  is strain rate sensitivity. When the material fails during processing,  $\eta$  may also be very high, so a higher  $\eta$  does not definitely mean that the material has more workability. Use the dimensionless parameter ( $\xi(\dot{\epsilon})$ ) to represent the rheological instability diagram during plastic flow (based on the Principle of Irreversible Thermodynamic Extremes), the instability criterion can be defined as follows [29]:

$$\xi(\dot{\epsilon}) = \frac{\partial[\lg(m/m+1)]}{\partial(\lg \dot{\epsilon})} + m < 0 \quad (8)$$

As shown in Fig. 6, the processing maps of the homogenized and pre-rolled samples can be superimposed by the power dissipation map, where shaded areas represent the instability region ( $\xi(\dot{\epsilon}) < 0$ ) and the contours lines which represent the power dissipation efficiency are marked as percent. It is easily observed that the main unstable windows are in a temperature domain between 370 °C and 480 °C with strain rate from 0.018 s<sup>-1</sup> to 3.1 s<sup>-1</sup> (Fig. 6 a, homogenized samples), or a temperature between 410 °C and 490 °C with strain rates from 0.03 to 0.316 s<sup>-1</sup> (Fig. 6 b, pre-rolled samples). Noticeably, DRX can easily occur in the region with higher power dissipation efficiency (0.39–0.51 for the homogenized sample, 0.32–0.47 for the pre-rolled one). Such regions at lower strain rates mean good workability. However, the unstable flow localization may also occur when the material is deformed at higher strains, so hot-working in these areas is not recommended.

Generally, the alloy hot-deformed in the condition with high efficiency of power dissipation shows good workability, and there are two high power dissipation domains for the homogenized sample. Figure 6 a shows that the first efficiency of power dissipation is about 21%, which is marked as domain A that appears in the temperature within 440 °C–460 °C and strain rate of 0.1 s<sup>-1</sup> (log  $\dot{\epsilon} = -1$ ). The other one with the highest efficiency of power dissipation is domain B with a value about 51%, which occurs in the temperature between 370 °C and 450 °C and strain rate of 0.01 s<sup>-1</sup> (log  $\dot{\epsilon} = -2$ ). This is the optimum region for

processing within the wide temperature range investigated in this work.

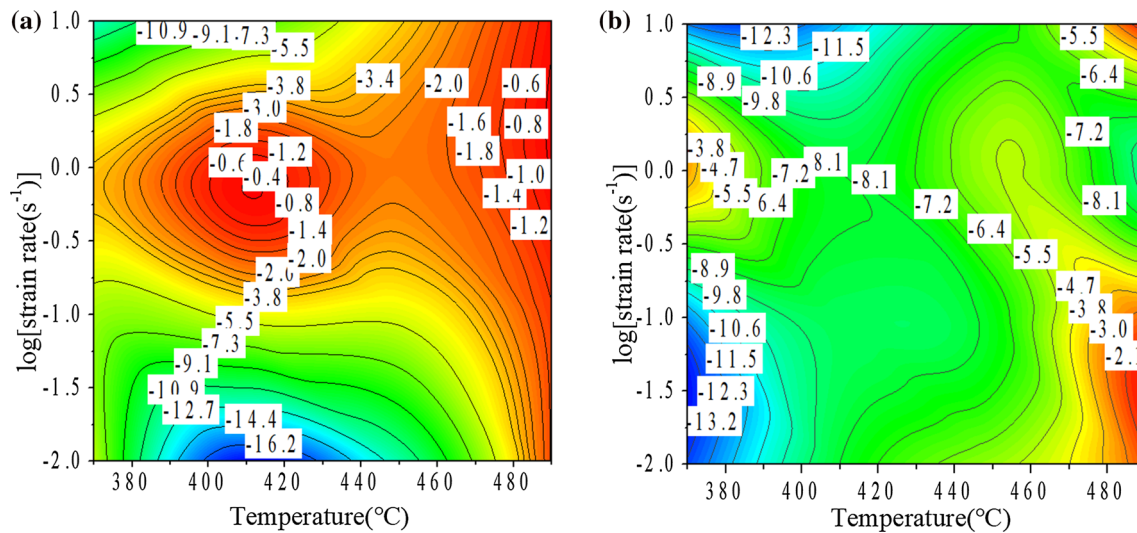
Another example given in Fig. 6 b for pre-rolled (ITMP) condition is the D regions, which is the most suitable processing domain with an efficiency of power dissipation about 47%. Domain D locates in temperature of 370–490 °C and strain rate from 0.01 s<sup>-1</sup> (log  $\dot{\epsilon} = -2$ ) to 0.03 s<sup>-1</sup> (log  $\dot{\epsilon} = -1.5$ ). In this processing map, the unstable regions are relatively of a lower area ratio, which indicates more ranges can be applied for a good hot workability.

### 3.4 Microstructural Evolution

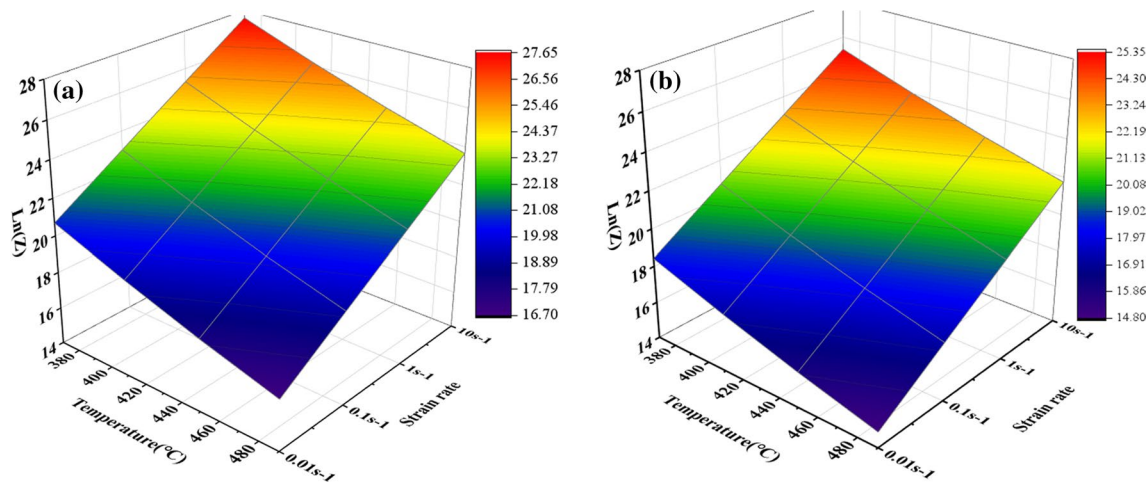
#### 3.4.1 Effect of Temperature on Microstructure

Figure 7 depicts the microstructure of deformed samples at different temperatures and examined using the EBSD method. As shown in Fig. 2, different initial microstructure exists in the homogenized (CTMP) and pre-rolled (ITMP) samples for the deformation at 370 °C and 490 °C with strain rates of 0.01 s<sup>-1</sup>. In an IPF maps, the boundary misorientation angles can be distinguished by the line colors: white lines: 2°–10°; red lines: 10°–15°; black lines: > 15°. It is evident from Fig. 7 a and b that for the formation of a number of low-angle boundary at low temperature, the compressed original grains become flat and elongated. This indicates a high density of cell and sub-grain structures, which results in a minority of DRX grains with HAGBs emerging beside the deformed grain boundaries (Fig. 7 b), and these LAGBs are caused by dislocation substructure which is induced by DRV. Another example is shown in Fig. 7 c and d, where the grains are notably equiaxed with increasing temperature. There are a large amount of high-angle boundaries associated with the formation of new grains by the discontinuous recrystallization, because the high deformation temperature can promote the grain boundary migration. Therefore, it accelerates the DRX during the deformation process. In addition, the grains shown in Fig. 7 a–d are found to be elongated after the hot deformation. The strong <110> fiber texture is formed in the samples, which is typical for face-centered cubic (FCC) metals after uniaxial compression. Fiber texture is reported to rotate only before and after the deformation [30, 31].

In order to figure out the effects of deformation temperature on the DRX for the samples with different initial microstructures, the changes of deformation microstructure is analyzed at different temperatures. The distribution of misorientation angle at the different deforming temperatures with a strain rate of 0.01 s<sup>-1</sup> is plotted in Fig. 7 e. It is noted that misorientation angles of 10–15° have a higher fraction in the ITMP process. It indicates the occurrence of continuous dynamic recrystallization (CDRX) for subgrains substructures [32]. Meanwhile, the fraction of misorientation > 15° is increasingly higher, which make the full



**Fig. 4** Decline ratio map at condition a true strain of 0.9 **a** CTMP and **b** ITMP



**Fig. 5** Color map of the relationship with  $\ln Z$  under various deformation conditions at condition a true strain of 0.9, **a** CTMP (homogenized) **b** ITMP (pre-rolled)

occurrence of DRX, i.e., the DRX degree is increased with increasing deformation temperature (Fig. 7 f).

The Fig. 8 a illustrates that the degree of recrystallization raises with the increasing of temperature between 370 and 490 °C, and the fraction of DRX of ITMP is higher than CTMP. Here, there is different microstructure for the initial materials of homogenized (CTMP) and pre-rolled (ITMP) processes. When the sample is deformed condition at a low deformation temperature, it will inflict the increase of dislocation density, pile-up, dislocation reduplication and tangle, where accumulated dislocations can remarkably hinder further deformation [33]. It is widely known that the driving force of dislocations is improved with increasing temperature, and this process promotes dynamic recrystallization

and dynamic recovery. However, aluminum alloys with high stacking fault energy are often softened dominantly by the way of DRV at low temperatures, while the occurrence of DRX can be found at a high temperature and low strain rate. Since the pre-rolled (ITMP) sample has been deformed to 50% after homogenization, this induces more sub-grain structure and dislocations than the homogenized (CTMP) one.

Then, the stored energy in deformed materials can be calculated through the analyses of LAGBs by two steps: First of all, the calculation of interface energies for boundaries  $> 2^\circ$ ; Secondly, the statistics of interface area per unit volume can be done as detailed by Godfrey et al.[34, 35]. As shown in Fig. 8 b, the value of stored energy for LAGBs



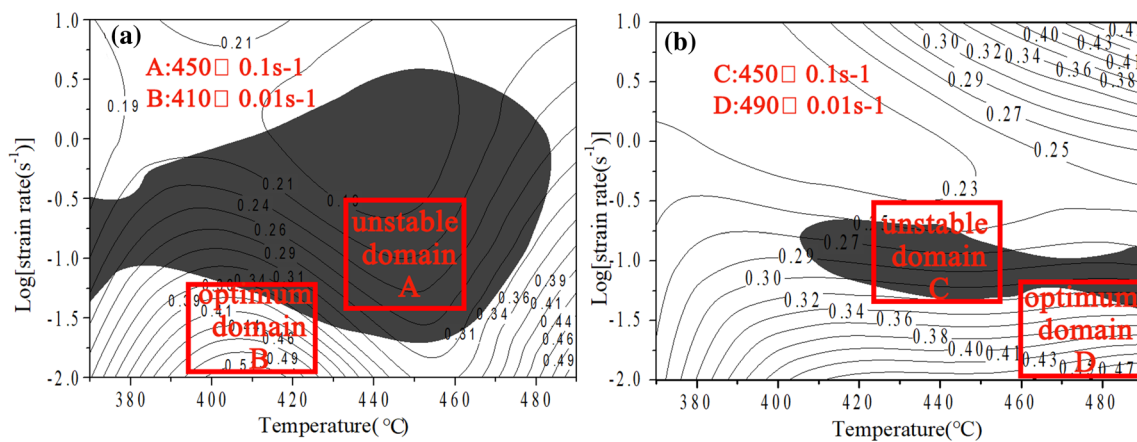


**Fig. 6** Processing maps for Li-containing aluminum alloys AA2060 at condition a true strain of 0.9 after **a** homogenized and **b** pre-rolled

decreases with the increase of recrystallization fraction, which is probably due to the difference in the stored energy evocable by the different level of restoration along with the changes of power dissipation efficiency ( $\eta$ ). The LAGBs stored energy of the samples deformed at 370 °C and 0.01 s<sup>-1</sup> are 87 kJm<sup>-3</sup> and 57 kJm<sup>-3</sup> for the ITMP and CTMP samples, respectively. The highest one among all four specimens indicates that the LAGBs fraction is highest. Moreover, the value of LAGBs stored energy should be able to response the level of DRX, i.e., the LAGBs stored energy decreases with the DRX increases. These explains why the degree of recrystallization for the pre-rolled samples are higher than for CTMP samples.

### 3.4.2 Microstructure Analysis based on Thermal Processing Map

Thermal processing maps can be generated for CTMP and ITMP processes from the stress—strain data obtained, and the appropriate process windows can be determined for hot deformation, according to the processing maps illustrated in Fig. 6. Two typical domains can be chosen to investigate the microstructure evolution process, i.e., domain A and C for an unstable region, domain B and D for an optimum processing region. The values of power dissipation ( $\eta$ ) are shown in the map as contour lines, and it reveals the relationship between microstructural evolution and power dissipation capacity. The peak  $\eta$  values of 0.5 and 0.47 appear at the optimum domains (near regime B, D in Fig. 6), respectively. Among them the corresponding parameter Z is the lowest. It suggests the occurrence of superplastic deformation for CTMP and ITMP routes. In addition, a relatively low  $\eta$  valued of 0.21 and 0.27 in domains A and C can be illustrated in Fig. 6, respectively. They are instability domains, for these cases adiabatic shear, flow localization, and kinking formation may occur.

The IPF maps reveal the microstructure for homogenized or pre-rolled specimens after deformation in the selected domains (Fig. 9). The boundary misorientation angles are still be distinguished by the line colors: white lines are of 2°–10°; red lines of 10°–15° and black lines of > 15°. In the unstable region A and C from Fig. 9 a and b, it is observed that kinking occurs in some large grains, and shear banding (marked by black ellipse and rectangles in Fig. 9 a and b) is also found in those regions between larger grains and finer grains. Due to strong texture in the face-centered cubic structure of Al alloys contained Li [31, 36], the flow localization (as the red arrows in Fig. 9 a and b) can be found in these deformed microstructure of elongated grain regions. However, in the optimum processing domain B, it can also be observed that the recrystallized grains are generated near the grain boundaries. The domain D of fully recrystallized grains indicates that the dislocation density is reduced to facilitate the further dislocation motion with the increase of temperature [20].

Generally speaking, in order to compute the effects of the unstable and optimum domains on misorientation gradient, the point to origin (cumulatively) misorientation distribution analysis can be performed within the grains of similar orientation to calculate along the border lines marked in Fig. 9 a, b, c and d. The misorientation profiles along the direction of A-line1 and B-line2 in different conditions are illustrated in Fig. 9 e, where the cumulative misorientation along A-line1 exceeds 10° at about a distance of 65  $\mu$ m, indicating that rotation of progressive sub-grains may occur in the deforming. From Fig. 9 f, both the cumulative misorientation along C-line1 and D-line2 cannot exceed 5°, which shows that the CDRX is under-developed if the deformation degree is relatively smaller [37], and the microstructure is relatively uniform after deformation.

The mechanisms for dynamic microstructure evolution in unstable domains and optimum processing domain

**Fig. 7** IPF maps of alloy AA2060 deformed condition at a strain rate of  $0.01\text{ s}^{-1}$  after different processes: **a** 370 °C and **c** 490 °C for the homogenized samples (CTMP Process); **b** 370 °C and **d** 490 °C for the pre-rolled sample (ITMP process); **e, f** Grain boundary misorientation

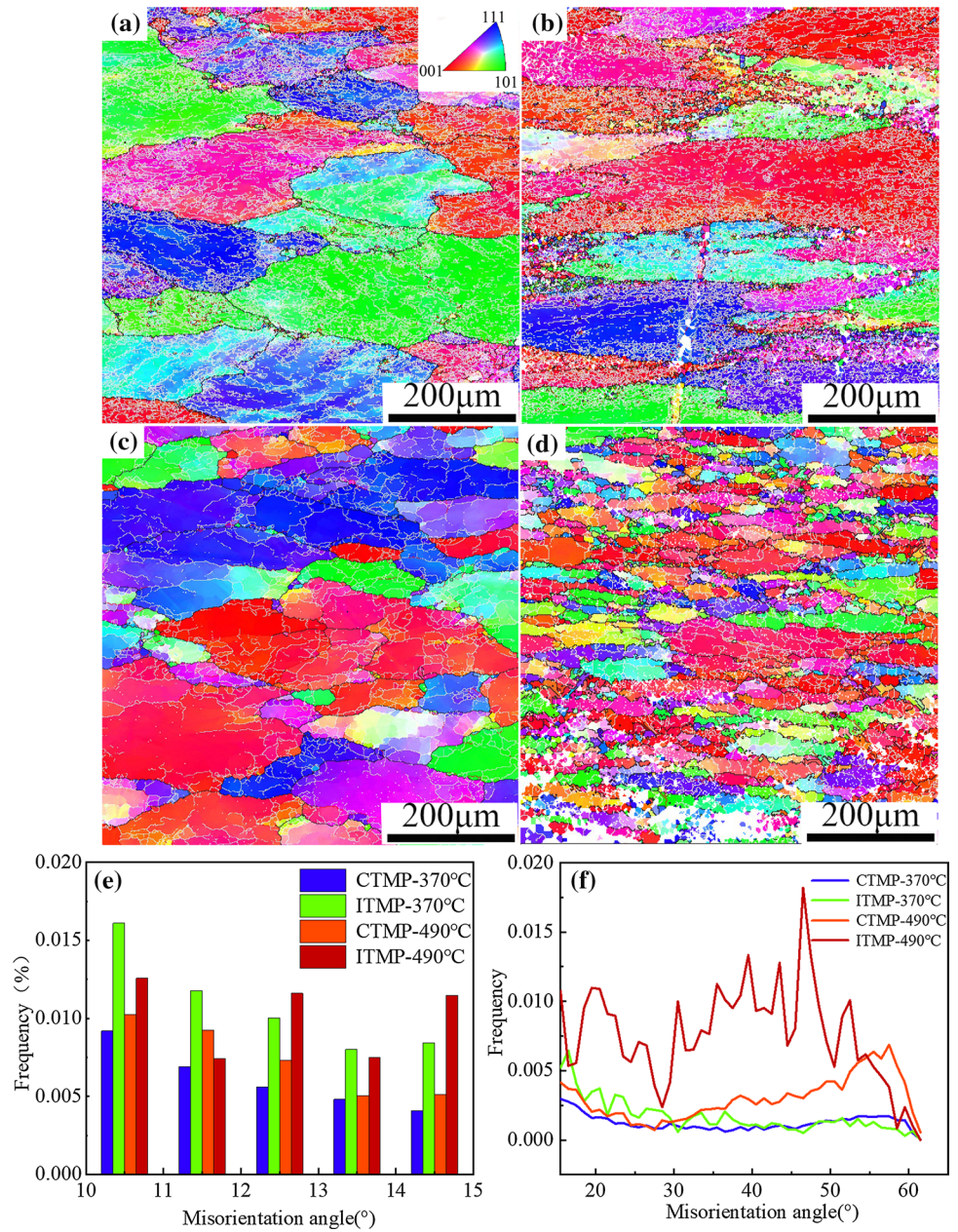


**Fig. 8** The degree of recrystallization **a** and LAGBs stored energy **b** of CTMP vs ITMP Process

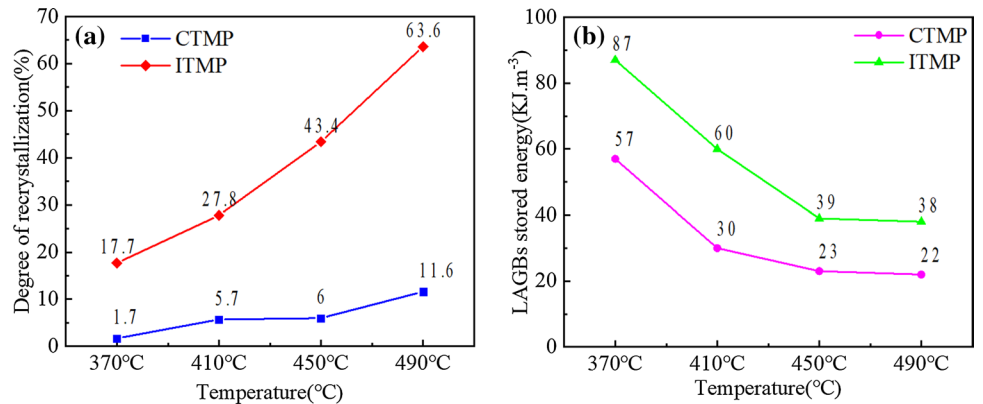
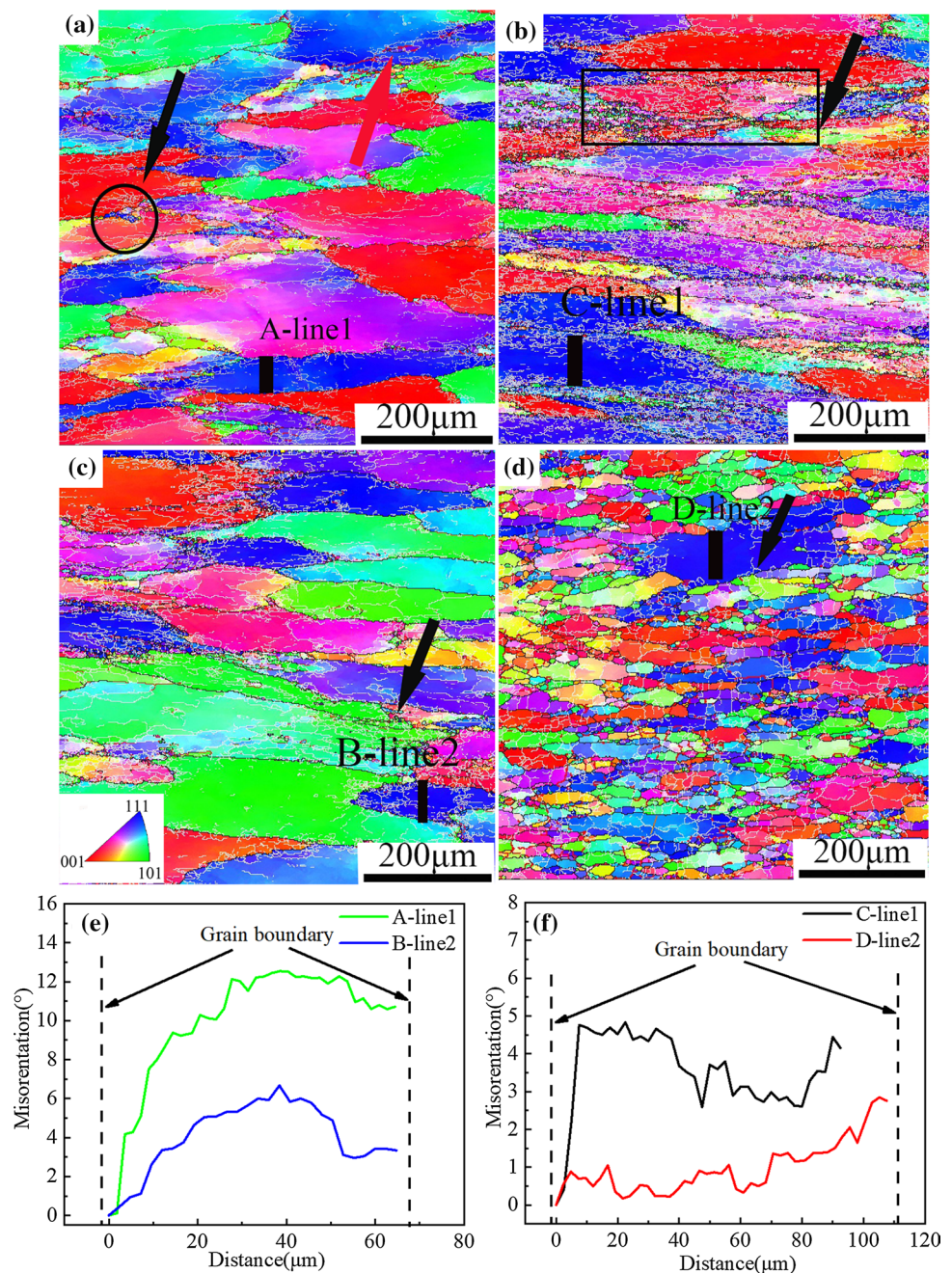


**Fig. 9** IPF maps for aluminum alloy AA2060 after **a, c** homogenized (CTMP) and **b, d** pre-rolled (ITMP), followed by deforming under different conditions: **a** and **c** at 450 °C and 0.1 s<sup>-1</sup>(region A,C); **b** at 410 °C and 0.01 s<sup>-1</sup>(region B), and **d** at 490 °C and 0.01 s<sup>-1</sup>(region D); **e, f** the point to origin (cumulatively) misorientation distribution corresponding to lines A,B,C and D in the grains in figures (**a, b, c** and **d**), respectively

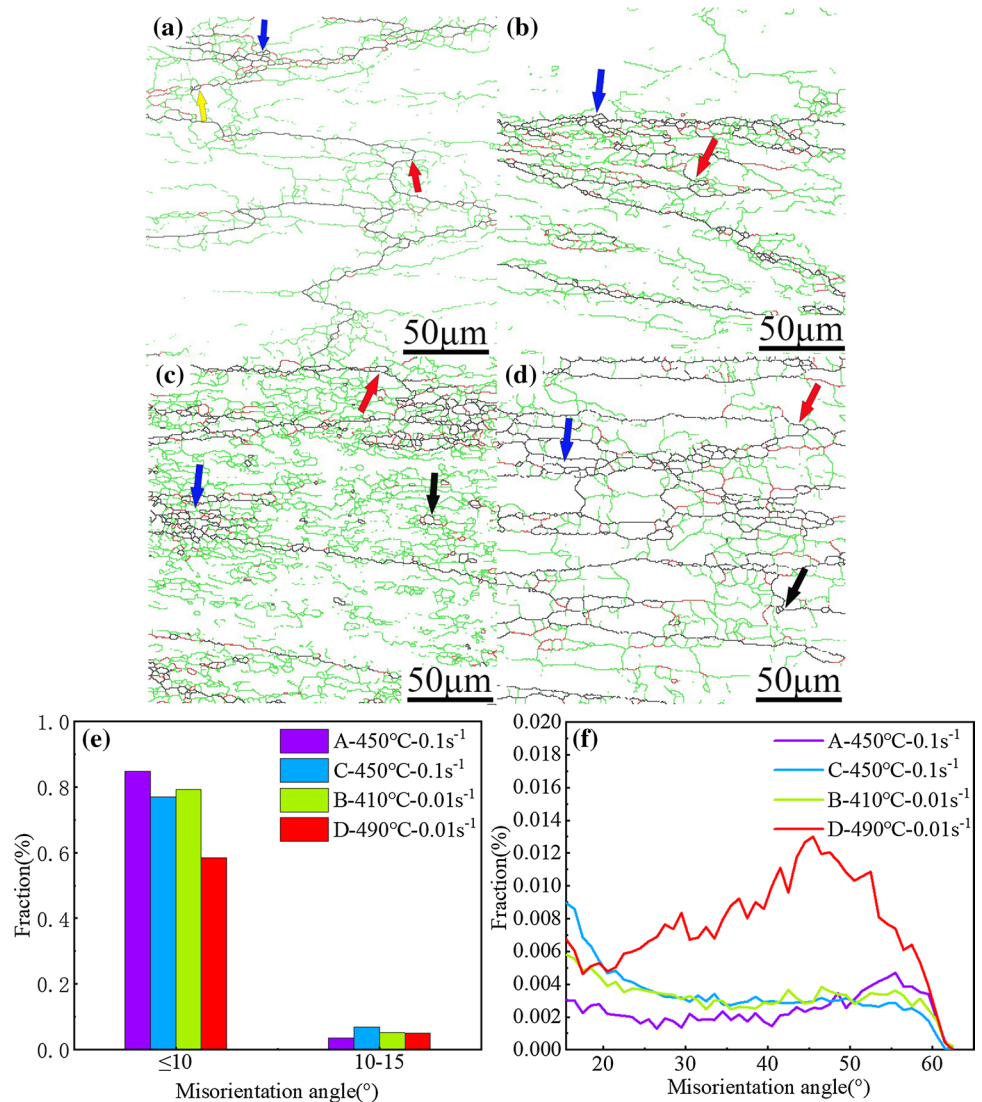


can be analyzed on the basis of Fig. 10. Huang et al. [38] reported that there are three kinds of DRX, which appears by progressive lattice rotation near grain boundary migration (GBM). Some studies also pointed out that progressive sub-grain rotation (SGR) is a symbol of CDRX [37], which can be observed in Fig. 10 a, b, c and d ( as pointed by blue arrows). To study the effect of sub-grain rotation in the nucleation of DRX, the fraction of misorientation angle under different hot-deforming conditions are summarized in Fig. 10 e. It can be found that the fraction of LAGBs ( $\leq 10^\circ$ ) of CTMP specimens are higher than ITMP specimens during hot deformation, while the fraction of

boundaries with  $10\text{--}15^\circ$  misorientation shows opposite tendency.

Moreover, according to Fig. 5 and Fig. 10 e and f, the distribution of misorientation angles transforms to higher angles with the decrease of  $\ln Z$ , i.e., the fraction of CDRX decreases with decreasing  $\ln Z$ . This is consistent with the analysis results in previous study [10]. The fraction of  $f_{LAGB}$  can be determined as 88.28% in the unstable domain A and 83.8% in the optimum processing domain B respectively. It can be determined that the average misorientation angles is  $7.6^\circ$  and  $8.9^\circ$  for the above two cases, respectively. The raise of average misorientation angle is interrelated to the

**Fig. 10** Grain boundary maps of the deformed alloy AA2060: **a, b** homogenized and **c, d** pre-rolled samples, which **a, c** are in instability windows, and **b, d** are in optimum processing windows, **e, f** are misorientation angle distribution



growth process of DRX nuclei [25,37,38]. In addition, it is noted that a large increase of approximately 10° for the average misorientation can be found in the optimum processing domain D. Therefore, the characteristic of CDRX is progressive sub-grain rotation due to an increased fraction of misorientation of 10–15° LAGBs in deformed samples. Subsequently, with the increase of misorientation angles, a number of LAGBs can be transformed into HAGBs [25]. In other words, the relative fraction of low-angle grain boundaries may decrease, as the high-angle grain boundaries become relatively higher than low-angle grain boundaries if the deformation condition changes. This can happen similarly in the homogenized sample. CDRX is characterized by grains consisting of HAGBs surrounded, and in the case it is not fully recrystallized, it is indicated that the formation of new grains is incomplete [39].

In the deformed samples reaching a certain critical strain, the DDRX occurs at the margins of existing grains

through local grain boundary bulging (BLG), which happens depending on the strain rate, deformation temperature and initial grain size of the materials. In this state, the microstructure is deformed to generate a “necklace” structure, and the microstructure for LAGBs migrates to form new grains [40], which has been widely acknowledged [23, 37]. In addition, the stress–strain curves show the transition from single to multiple peaks [27], which has been found in both hot-deformed and homogenized specimens (red arrow in Fig. 10 a and b). However, for the deformed and pre-rolled specimens, a great deal of sub-grains (the green and red lines in Fig. 10 a, b, c and d) can be found. As they are orientated in initial structure before deformation, it can affect DDRX via deformation conditions (temperature, strain rate etc.).

Additionally, in the recent work of J. K. Solberg et al. [41] about geometric dynamic recrystallization (GDRX) mechanisms, it indicates that the original grains can split into new grains as a result of high strain deformation. During

deformation, apposite strain rate introduces a high defect density, which leads to the formation of sub-grain cell dislocation. The grains can form internal sub-grains. When the grains continue to be deformed, these sub-grains can “break out” their parent grains, and the concave serrations of the original boundaries will contact sub-grains. New grains are finally formed and some smaller grains are consisting of original high-angle grain boundary. This mechanism of GDRX was reported [42], and the related phenomenon is shown by the yellow arrow marked in Fig. 10 a.

In order to study the effect of sub-grain rotation on the nucleation of dynamic recrystallization, the fraction of misorientation angle in different domains is varied. For example, the fraction of grain boundary misorientation angles above  $15^\circ$  can be found in Fig. 10 f. When the pre-rolled specimen is deformed at low strain rates and high temperature, a great deal of LAGBs grows into HAGBs and generate the fully recrystallized grains. The grains may form from the original sub-grains in pre-rolled condition, instead of the homogenized sample, which indicates that the multiple deformation forms a large number of sub-grains for the possible occurrence of meta-dynamic recrystallization (MDRX) [43]. (highlighted by the black arrow in Fig. 10 c).

In summary, the mechanism of dynamic recrystallization can be divided into four categories, namely, CDRX, DDRX, GDRX, and MDRX. The CDRX and DDRX mechanisms are possibly to occur in both homogenized and pre-rolled samples, but the GDRX only occurs in the homogenized materials during hot deformation. In addition, the MDRX mechanism also only happens in pre-rolled and deformed condition. Based on these DRX microstructure characteristics, the statistical results are illustrated as histogram in Fig. 11 a.

In order to further investigate and reveal schematic of the DRX mechanism, the grains are divided into different kinds based on their processing parameters. As shown in Fig. 11 b, it is noted that DDRX is the mainly mechanism in the unstable domain, but the CDRX mechanism appears in the optimum processing domain. The GDRX only occurs in the unstable domain. Combining the results above, the

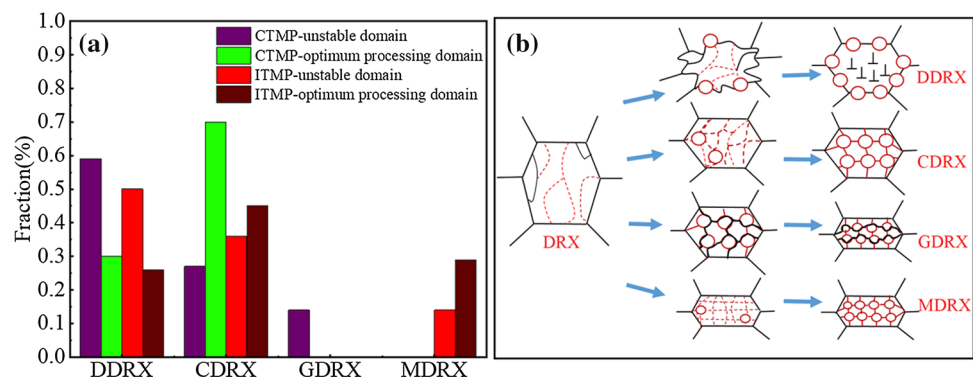
DRX mechanism is relevant to the relative softening rate  $M_s$  and  $\ln Z$  parameter. Lower values of relative softening rate  $M_s$  and  $\ln Z$  parameter Lead to an easy occurrence of DRX.

## 4 Conclusions

Aluminum alloy AA2060 with different initial microstructure was hot deformed at temperature between  $370^\circ\text{C}$  and  $490^\circ\text{C}$  and strain rates range of  $0.01\text{--}10\text{ s}^{-1}$ . The effect of strain stress, deformation temperature, processing maps, and microstructural evolution were analyzed. Some conclusions of this work can be obtained as follows:

- (1) During hot deformation at  $370^\circ\text{C}$  and  $490^\circ\text{C}$  with a same strain rate of  $0.01\text{ s}^{-1}$ , the flow stress of both homogenized and pre-rolled specimens decreases with increasing temperature, and the flow stress of the homogenized one is higher than for the latter at the same strain rate and temperature.
- (2) The activation energy associated with the hot workability for the homogenized or pre-rolled and deformed samples is  $135.2\text{ kJ/mol}$  and  $123.1\text{ kJ/mol}$ , respectively.
- (3) The recrystallization fraction in both samples deformed at  $370\text{--}490^\circ\text{C}$  and  $0.01\text{ s}^{-1}$  is increased with increasing deformation temperature. The fraction of recrystallization of pre-rolled and deformed sample is higher than for the homogenized and deformed specimens. However, the value of LAGBs stored energy changes with the deformation temperature between  $370^\circ\text{C}$  and  $490^\circ\text{C}$  oppositely.
- (4) The dynamic recrystallization mechanisms can be divided into four types, i.e., CDRX, DDRX, GDRX, and MDRX for both samples. The GDRX only occurs in the homogenized materials. Meanwhile, the MDRX also only happens in pre-rolled and deformed condition. The decline ration of flow stress  $M_s$  and  $\ln Z$  correspond to the various softening mechanisms and workability.

**Fig. 11** The DRX of alloy AA2060 maps for: **a** The proportion of recrystallization in CTMP and ITMP process deformed specimens; **b** Schematic illustrations showing the DRX behavior



**Acknowledgements** The authors acknowledged the financial support by the National Natural Science Foundation of China (51421001); the Open Fund of National Key Laboratory of Science and Technology on High-strength Structure Materials, Central South University; and the Fundamental Research Funds for the Central Universities (2020CDJDCL001).

## Declarations

**Conflicts of interest** The authors declare no conflict of interest.

## References

- R.J.H. Wanhill, G.H. Bray, Chapter 2-Aerostructural Design and Its Application to Aluminum-Lithium Alloys. in *Aluminumlithium Alloys, Processing, Properties and Applications*, ed. by N.E. Prasad, A.A. Gokhale, R.J.H. Wanhill Butterworth-Heinemann (Butterworth-Heinemann, Oxford, 2014), pp. 27–58
- A.A. El-Aty, Y. Xu, X.Z. Guo, S.H. Zhang, Y. Ma, D.Y. Chen, J. Adv. Res. **10**, 49 (2018)
- X. Sheng, L.D. Yang, Z.R. Hua, L.J. Feng, C.Y. Lai, Z.X. Hu, T. Nonferr. Metal. Soc. **25**, 3855 (2015)
- Z. Fei, S. Jian, Y.X. dong, S.J. Iin, Rare Metal. Mat. Eng. **43**, 1312 (2014)
- X. Huang, H. Zhang, Y. Han, W. Wu, J. Chen, Mater. Sci. Eng. A **527**, 485 (2010)
- H.Z. Li, Z. Li, M. Song, X.P. Liang, F.F. Guo, Mater. Design **31**, 2171 (2010)
- O. Ling, Z.Q. Zheng, Y.F. Nie, H.G. Jian, J. Alloy. Compd. **648**, 681 (2015)
- R. Zhu, Q. Liu, J. Li, S. Xiang, Y. Chen, X. Zhang, J. Alloy. Compd. **650**, 75 (2015)
- Q. Yang, X. Wang, X. Li, Z. Deng, Z. Jia, Z. Zhang, G. Huang, Q. Liu, Mater. Character. **131**, 500 (2017)
- L.F. Cao, B. Liao, X.D. Wu, C.Y. Li, G.J. Huang, N.P. Cheng, Curr. Comput.-Aid. Drug **10**, 416 (2020)
- W.C. Yu, H.Y. Li, R. Du, W. You, M.C. Zhao, Z.A. Wang, Mater. Character. **145**, 53 (2018)
- G. Avramovic-Cingara, D.D. Perovic, H.J. McQueen, Metall. Mater. Trans. A **27**, 3478 (1996)
- L.Y. Ye, X.M. Zhang, Y.W. Liu, J.G. Tang, D.W. Zheng, Mater. Sci. Technol. **27**, 125 (2011)
- T.J. Ruggles, D.T. Fullwood, Ultramicroscopy **133**, 8 (2013)
- W.X. Ya, J.J. Tang, L.G. Ai, W.X. Ming, S. Jian, Z. Liang, J. Alloy. Compd. **815**, 152469 (2020)
- J. Humphreys, G.S. Rohrer, A. Rollett, Chapter 9 - Recrystallization of Two-Phase Alloys, in *Recrystallization and Related Annealing Phenomena*, 3rd ed. (Elsevier, Amsterdam, 2017), pp. 321–359
- H.J. McQueen, Mater. Sci. Eng. A **387–389**, 203 (2004)
- C.J. Shi, J. Lai, X.G. Chen, Materials **7**, 244 (2014)
- Y. Wang, G. Zhao, X. Xu, X. Chen, C. Zhang, J. Alloy. Compd. **779**, 735 (2019)
- C.M. Sellars, W.J.M. Tegart, Acta Metall. **14**, 1136 (1966)
- H.L. He, Y.P. Yi, J.D. Cui, S.Q. Huang, Vacuum **160**, 293 (2019)
- B. Li, Q. Pan, Z. Yin, Mater. Sci. Eng. A **614**, 199 (2014)
- B. Shen, L. Deng, X. Wang, Mater. Sci. Eng. A **625**, 288 (2015)
- X. Yang, W. Huang, X. Zhu, R. Zhang, F. Guo, L. Hu, Met. Mater. Int. (2020). <https://doi.org/10.1007/s12540-020-00800-y>
- S.V. Mehtonen, L.P. Karjalainen, D.A. Porter, Mater. Sci. Eng. A **571**, 1 (2013)
- Y.V.R.K. Prasad, H.L. Gegel, S.M. Doraivelu, J.C. Malas, J.T. Morgan, K.A. Lark, D.R. Barker, Metall. Trans. A **15**, 1883 (1984)
- X.-X. Yu, Y.-R. Zhang, D.-F. Yin, Z.-M. Yu, S.-F. Li, Acta Metall. Sinica Engl. **28**, 817 (2015)
- G.J. Reddy, N. Srinivasan, A.A. Gokhale, B.P. Kashyap, J. Mater. Process. Tech. **209**, 5964 (2009)
- Y.V.R.K. Prasad, Indian J. Technol. **28**, 435 (1990)
- H. Garmestani, S. Lin, B.L. Adams, S. Ahzi, J. Mech. Phys. Solids. **49**, 589 (2001)
- A. Ma, F. Roters, Acta Mater. **52**, 3603 (2004)
- S. Mandal, A.K. Bhaduri, V.S. Sarma, Metall. Mater. Trans. A **42**, 1062 (2011)
- W.J. He, C.H. Li, B.F. Luan, R.S. Qiu, K. Wang, Z.Q. Li, Q. Liu, T. Nonferr. Metal. Soc. **25**, 3578 (2015)
- A. Godfrey, W.Q. Cao, Q. Liu, N. Hansen, Metall. Mater. Trans. A **36**, 2371 (2005)
- A. Godfrey, N. Hansen, D.J. Jensen, Metall. Mater. Trans. A **38**, 2329 (2007)
- X. Yang, W. Huang, X. Zhu, F. Guo, Y. Ma, L. Chai, R. Zhang, Met. Mater. Int. (2020). <https://doi.org/10.1007/s12540-020-00670-4>
- Y.C. Lin, X.Y. Wu, X.M. Chen, J. Chen, D.X. Wen, J.L. Zhang, L.T. Li, J. Alloy. Compd. **640**, 101 (2015)
- K. Huang, R.E. Logé, Mater. Design **111**, 548 (2016)
- A. Halfpenny, J. Prior, P.J. Wheeler, Tectonophysics **427**, 3 (2006)
- I. Shimizu, J. Struct. Geol. **30**, 899 (2008)
- J.K. Solberg, H.J. McQueen, N. Ryum, E. Nes, Philos. Mag. A **60**, 447 (1989)
- H.R. Rezaei Ashtiani, M.H. Parsa, H. Bisadi, Mater. Design **42**, 478 (2012)
- M.H. Maghsoudi, A. Zarei-Hanzaki, P. Changizian, A. Marandi, Mater. Design **57**, 487 (2014)

**Publisher's Note** Springer Nature remains neutral with regard to jurisdictional claims in published maps and institutional affiliations.